Journal of the European Ceramic Society **17** (1997) 1485–1500

PII: S0955-2219(97)00004-6
0955-2219/97/$17.00

Carbon-Fibre-Reinforced (YMAS) Glass–Ceramic Matrix Composites. I. Preparation, Structure and Fracture Strength

Valérie Bianchi,[a] Paul Goursat,[a] Wharton Sinkler,[b]
Marc Monthioux[b] & Erik Ménessier[c]

[a]LMCTS, URA CNRS 320, Faculté des Sciences, 123, Avenue Albert Thomas, 87060 Limoges Cedex, France
[b]CEMES, UPRESA 6015 CNRS, B.P. 4347, 31055 Toulouse Cedex, France
[c]Céramiques et Composites, B.P. 7, 65460 Bazet, France

(Received 9 July 1996, revised version received 29 July 1996, accepted 2 December 1996)

Abstract

Unidirectional continuous carbon-fibre-reinforced glass–ceramic matrix composites are fabricated for dry sliding applications. The microstructure of the matrix has been characterized by X-ray diffraction and the microtexture and structure of the fibres (pitch-based and PAN-based) have been studied by transmission electronic microscopy. The different fracture behaviours of the composites are described (three-point bend test and fracture surface observation by scanning electronic microscopy). Due to the thermal expansion mismatch between the fibres and the matrix, a network of microcracks appears in the composites on cooling after hot-pressing. The relationship between the microcrack spacing and the fracture behaviour suggests modifications of the fibre–matrix bond. © 1997 Elsevier Science Limited.

Des composites unidirectionnels á fibres longues de carbone et matrice vitrocéramique sont élaborés pour des applications en frottement sec. La microstructre de la matrice est suivie par diffraction des rayons X. La micro-texture et la microstructure des fibres (ex-brai et ex-PAN) sont étudiées en Microscopie Electronique en Transmission. Les différents comportements á la rupture des composites sont ensuite décrits (essais en flexion trois points et observation des fractures en Microscopie Electronique á Balayage). Du fait des différences de dilatation thermique entre les fibres et la matrice, un réseau de fissures apparaît au refroidissement dans les composites lors de leur frittage sous charge. La relation entre le pas de fissuration et le comportement à la rupture des composites suggère une évolution de la liaison fibre–matrice.

1 Introduction

During the last decades, the development of the aerospace industries has promoted research on new materials that combine lightness and favourable thermomechanical properties. Monolithic ceramics meet these requirements and are able to endure high temperatures and corrosive atmospheres but their applications are limited by their brittleness and their low toughness. It has been demonstrated that continuous fibres in ceramic matrix composites (CMCs) prevent catastrophic failure by giving them non-linear mechanical behaviour. Carbon-fibre-reinforced glass-matrix composites have been studied for a long time because of their very interesting thermomechanical properties. [1–3] Subsequently, the use of SiC fibre for strengthening a ceramic matrix has allowed applications in air at moderate temperatures to be considered. In particular, SiC-fibre-reinforced YMAS matrix composites have been proved to be very strong with a controlled fracture.[4] Similarly, monolithic ceramics could be used for wear applications but again their brittleness and their friction coefficient restrict their development. For this reason researchers are more and more concerned with the use of solid lubricants and ceramic composites in which carbon fibres could contribute their lubricant properties. However, many other factors must be considered and are of great importance, such as the geometry of the contact between the mechanical parts, the formation and the evolution of a third body from mechanical or physicochemical reactions at the interface.

This paper, which concerns the fabrication of unidirectional continuous carbon-fibre reinforced YMAS glass–ceramic matrix composites for dry

sliding uses,[5] is essentially devoted to the study of the carbon fibres as affected by sintering, to the microstructural changes of the YMAS (Y_2O_3, MgO, Al_2O_3, SiO_2) matrix and to the mechanical behaviours of the materials according to the thermal treatments.

2 Materials and Experimental Procedure

2.1 Carbon fibres

Three grades of fibre differing with respect to precursor and their final properties, pitch-based fibres (Thornel P25 and P55) and a PAN-based fibre (Torayca T400H) were used. Some properties of these fibres are reported in Table 1.

It is well known that the overall texture for any carbon fibre is highly anisotropic, with the graphenes (1 polyaromatic layer = graphene) oriented parallel to the fibre axis. However, the parallelism may be better or worse depending on the fabrication process and specifically on parameters such as the precursor and/or the final carbonization temperature. In contrast, the textural aspects of fibres may be much more variable when seen on cross-sections, also depending on the fabrication process, and specifically on parameters such as the precursor (pitch or PAN, pitch grade, ...) and/or the spinneret geometry. In addition, changes in texture may also be found within a given fibre grade because of changes in the fabrication process that the manufacturer may have decided to introduce at some time without changing the trade name. This may explain, for instance, why cross-sections of T300 fibre from Torayca are nowadays found to exhibit some anisotropic features,[6,7] while this was never reported in the 1980s.[8] Accurate characterization of the transversal texture of fibres used as reinforcement for the composites is therefore important.

2.1.1 Investigation methods

The micro- and nanotextural (isotropy, anisotropy, porosity, ...) and structural (crystallinity, defects, ...) study was mainly performed with a transmission electron microscope (Philips CM12 TEM), using a 120 kV high voltage and a Supertwin objective stage. The microscope was also equipped with energy dispersive analysis of the X-ray system (EDAX), which was used to perform local and comparative chemical analysis on areas larger than 50 nm and for elements with $Z > 5$.

Table 1. Characteristics of fibres (given by the manufacturers)

	Fibre		
	P25	*P55*	*T400H*
Longitudinal tensile strength (MPa)	1400	1900	4500
Longitudinal tensile modulus (GPa)	160	380	250
Tensile fracture elongation (%)	0·9	0·5	1·8
Density (g/cm^3)	1·90	2·0	1·80
Filament diameter (μm)	11	10	7
Number of fibres per tow	2000	2000	3000

2.1.2 Preparation of samples prior to investigations

As-received carbon fibres were prepared either by thin-sectioning of single filaments using a microtome (LKB Ultrotome) equipped with a diamond knife (MS Type from DIATOME) or ion-thinning of fibre tows according to the procedure described hereafter. Prior to both the preparation methods, samples were embedded in an epoxy resin (TAAB or POLARBED 812).

Small pieces of resin-embedded fibre tows were trimmed then mechanically thinned using diamond tools, then diamond and SiC powder suspensions and abrasive papers. The final step of mechanical thinning was performed on both sample faces using a dimple grinder (GATAN 656) with a diamond powder suspension (grain sizes were in the 2–4 μm range), in order to reach thicknesses close to about 30 μm. Thereafter, ion-thinning was performed (GATAN Duomill 600) using a 4 kV voltage and incidence angles from 20 to 12°.

2.1.3 Results

2.1.3.1 P55 fibres. The P55 fibres present a 'Pan-Am' texture[9] similar to that already found for P55S and P75 AMOCO fibres[10] with internal decohesions between polyaromatic sheets which certainly originate in the structural shrinkage occurring during the final carbonization step, during which superimposed graphene layers always tend to move closer together with increasing temperature in any carbon materials (the lower limit is that of the interlayer distance for graphite — 0·335 nm — which is, however, practically never reached in commercial carbon fibres).

Electron microscopy allows textural heterogeneities to be revealed. Specifically, large anisotropic areas (i.e. made of graphenes roughly oriented in a common direction at a long distance) exhibit numerous and small (≈ 100 nm) inclusions of isotropic (microporous) areas (i.e. made of graphenes with no preferred orientation, arrow in Fig. 1). In addition to the textural difference, the graphene stacks in the isotropic areas are less structurally organized, as shown by the lack of Bragg fringes (Bragg fringes originate from high order Bragg reflections which are stopped by the objective aperture and therefore make well-ordered phases appear locally darker in bright field imaging mode). As a matter of fact, higher magnifications

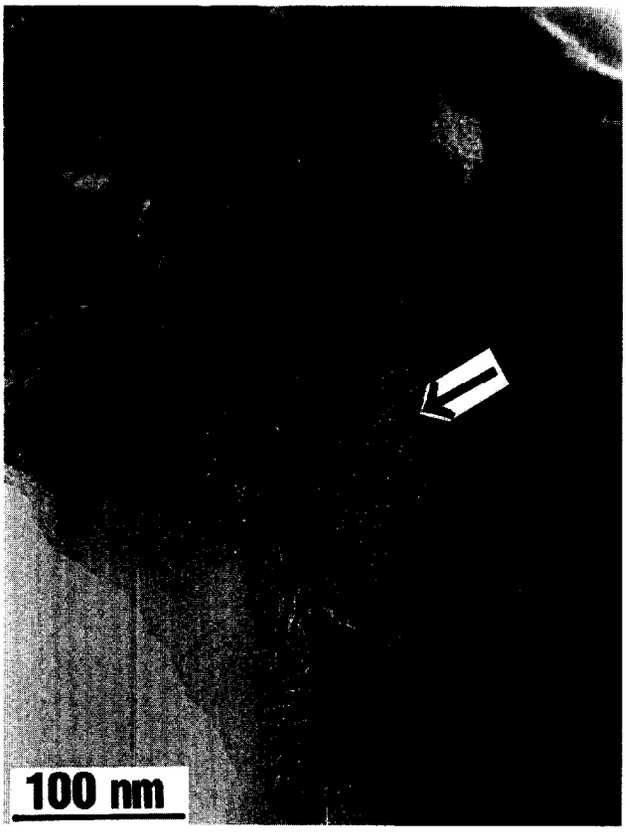

Fig. 1. P55 fibre cross-section. Bright field TEM image. White areas within anisotropic (dark) areas are decohesions between polyaromatic sheets. The grey part (arrow) is an isotropic inclusion.

(Fig. 2) illustrate the structural difference between the isotropic (above) and the anisotropic (below) regions. In as much as the crystalline order is biperiodic only (in contrast to genuine graphite), the structural state of such polyaromatic carbon materials, so-called turbostratic, may be characterized by the average lateral extension L_a of graphenes and the average number N of graphenes stacked. N and L_a thus define the average polyaromatic entity which may be considered coherent relative to the diffraction electron beam. Regarding the structural difference between the isotropic and the anisotropic parts in the fibre, L_a and N are 3–5 nm and 4–8, respectively, for the former, while N may reach 40–50 and L_a may reach 10 nm for the latter. Each entity is somewhat misoriented relative to the neighbouring entities, and separated from them by grain boundaries.[11] In addition, Fig.2 illustrates some details of Bragg fringes (arrows) and also how decohesions may occur within anisotropic areas (clear zones between aromatic sheets). An important feature, demonstrated by investigations on longitudinal sections of fibres (not illustrated), is that the microporous (isotropic) areas are not spherical but cylindrical inclusions within the fibre, more or less flattened, with the cylinder axis being parallel to the fibre axis. Such a textural heterogeneity is due to chemical heterogeneities within the pitch precursor.[12] As a general rule for the thermal behaviour of polyaromatic carbon phases, the microporous part will always stay far from the structural state of genuine graphite, whatever the heat-treatment temperature. In contrast, the anisotropic parts are more likely to evolve towards the graphite structure (without ever reaching it, however), and are responsible for the relatively high modulus value and low ultimate strength and strain of the P55 fibre relative to the PAN-based T400H fibre (Table 1). Finally, TEM observations (Figs 2 and 3) show that the directions of preferred orientations may vary greatly at a scale of a hundred nanometers and lower, which is not in the resolution range for optical microscopy (about 0.5 μm). Hence, the Pan-Am texture revealed by optical microscopy[9] is only an average statistical tendency.

At the fibre surface, a third texture often occurs. It is made of very stiff (i.e. free of misorientations) graphene sheets which act as an incomplete coating around the fibre. The structural organization is very good: N may be 50 or more and L_a may reach 100 nm (Fig.3). Such a carbon skin is not systematic and does not adhere well to the fibre either.

2.1.3.2 P25 fibres. Low magnification TEM images show that the fibre surface may appear either smooth (Fig. 4(a)) or corrugated (Fig 4(b)). Generally speaking, the textural and chemical features of the P25 fibres are similar to those of P55 fibres when observed by TEM, i.e. a combination of isotropic and anisotropic areas and a highly anisotropic but incomplete polyaromatic carbon skin. However, the structures are similar but actually not identical. Indeed, the structural organization of graphene stacks is lower, as clearly revealed by high resolution imaging (Fig. 5). The number N of graphenes stacked into coherent entities is in the 5–10 range and their extension L_a (within anisotropic domains) is most often 2–3 nm (as compared to 40–50 and 10 nm, respectively, for the P55 fibre). A consequence is that grain boundaries are more numerous than in P55 fibres, since the coherent entities are smaller, which induces a higher ultimate strength value (Table 1). Indeed, the higher the number of boundaries, the higher the number of linking sites preventing the easy gliding between two superimposed graphenes. For the same reason, the bulk modulus of the P25 fibre is lower than the P55 fibre

Finally, the features are all consistent with the fact that P25 fibres originate from the same precursor and have undergone the same fabrication process as P55 fibres, but with a lower final carbonization temperature. This explains why the

interlayer decohesions, usual in P55 fibres (Fig. 2), have not occurred in P25 fibres (Fig. 5), since the structural shrinkage has not been intense enough.

2.1.3.3 T400H fibres. The overall molphology of the cross-sections may be round, oval or bean-shaped, with diameters in the 6–8 μm range and a ring evidenced at about half or third of the radius (Fig. 6(a)). This feature is consistent with previous observations performed on the T300 grade of PAN-based fibres from Torayca which exhibit a coarsely isotropic texture with a local anisotropic radial texture in the ring.[6,7] A possible explanation is that this is an effect of the mechanical stretching imposed on the green fibres during the spinning

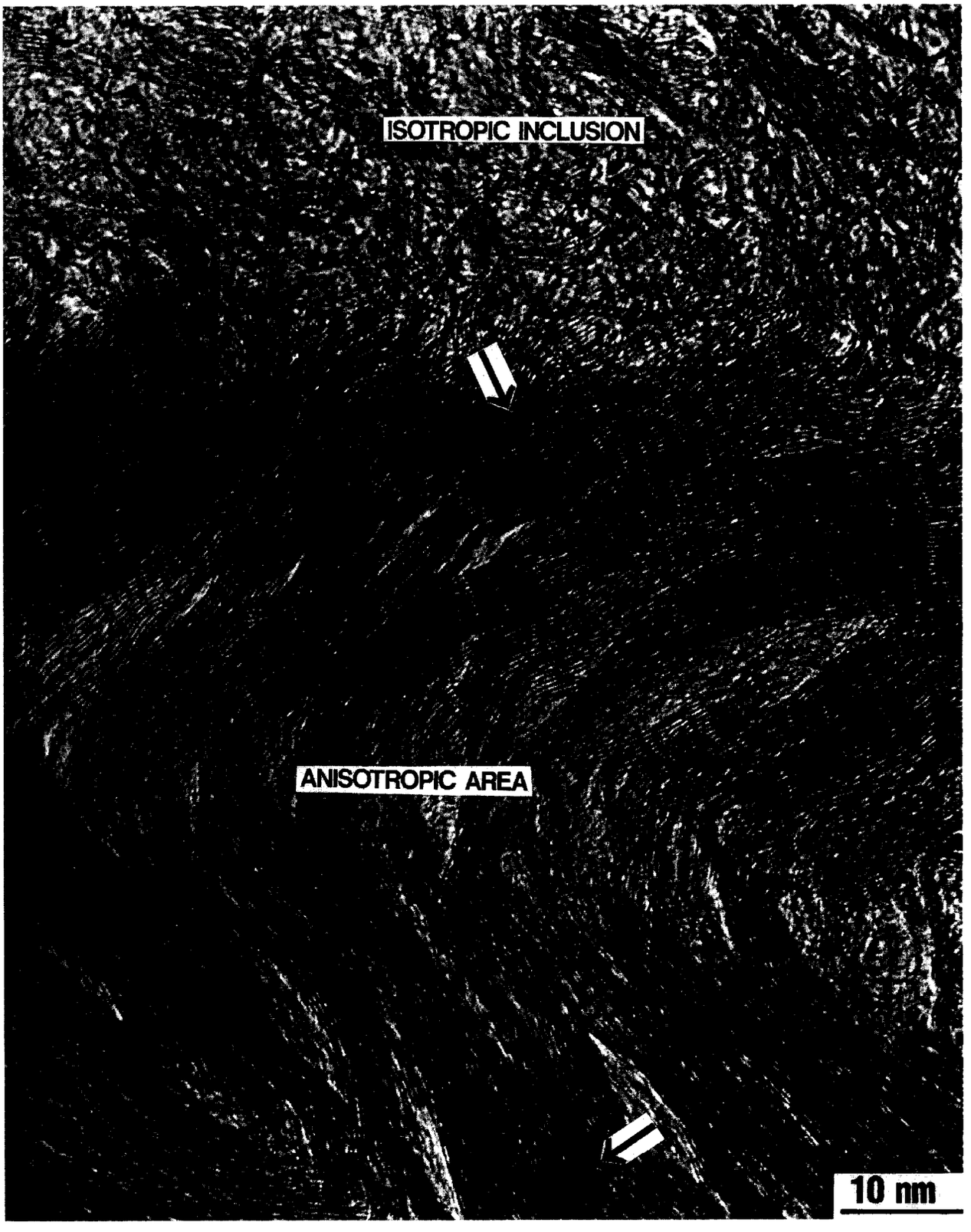

Fig. 2. P55 fibre cross-section. Lattice fringe TEM image. Above is an enlarged view of an isotropic area. Below is an enlarged view of an anisotropic area. Arrows illustrate Bragg fringes.

step, which may induce internal compressive/tensile stress discrimination, in association with the radial oxygen gradient developed during the subsequent curing and carbonization step.[13] Based on non-convincing TEM observations, the same authors have proposed a twinned radial/concentric texture for the dark ring in T300 fibres. This is unlikely for several reasons. Among others, we succeeded in revealing a radial orientation in high resolution imaging (see below), and never a concentric one.

Low magnification TEM images provide information on the fibre surface roughness (Figs 6(a) and 6(b)). The surface is rougher than that of the P25 and P55 fibres, and is consistent with the previous investigations performed on T300 fibres.[7,13] High resolution TEM imaging allows the nanotextural and structural aspects to be described (Fig. 7). The structural organization is very poor, since N is about 3–7 and L_a is about 1–3 nm. These features are close to that of P25 fibres, but a major difference is the lack of long range anisotropy (in cross-section). Another specific feature is the occurrence of round pores (arrow in Fig. 7) which are found in any T400H fibre, preferentially in areas close to the fibre surface (arrows in Fig. 6(b)). They pre-exist within the fibre, i.e. they are not induced by the preparation procedure for the TEM investigations, for instance, since they are not found in other ion-thinned PAN-based fibres from another source but are quite similar in other respects.[7] Such holes probably originate from some outgassing event occurring within the fibre when still softenable, at the first steps of the fibering process. Furthermore, this observation is again similar to previous investigations on T300 fibres[7,13] or T400H fibres[9] which, in addition, have demonstrated[7,9] that the pores are consistently cylindrical instead of spherical, with their axis oriented parallel to the fibre axis. High resolution imaging (Fig. 8) also reveals that the only anisotropic domain is encountered within the ring (which appears dark in low magnification images: Fig.6(a)) where the overall orientation of graphenes is perpendicular to the fibre surface (radial texture). In addition, the graphene stacks have a better structural organization than within the surrounding isotropic part of the fibre.

The textural and structural features of the T400H fibre explain the mechanical properties (Table 1). For the same reasons as those given for the P55/P25 fibre comparison, the ultimate strength is the highest, while the elastic modulus is low.

2.2 YMAS glass–ceramic matrix

The glass powder is obtained by mixing oxides (Y_2O_3, MgO, Al_2O_3, SiO_2), melting, cooling and grinding to obtain a grain size lower than 10 μm. The content of each oxide is chosen to yield, after the thermal treatment of the glass, a glass–ceramic mainly consisting of cordierite, yttrium silicates and a small quantity of the $MgAl_2O_4$ spinel phase.

The glass transition (T_g) and crystallization (T_c) temperature intervals have been determined by

Fig. 3. P25 or P55 fibre cross-section. Lattice fringe TEM image. Example of the very well-structured polyaromatic carbon phase found at the fibre surface.

differential thermal analysis (DTA) of the glass powder (Setaram Micro ATD M5—linear increase of 5°C/min), as 815–855°C and 945–1055°C, respectively.

The coefficients of thermal expansion (CTE) of the glass and the glass-ceramic have been measured with a vertical dilatometer (Setaram TMA 92), in argon, with a linear heating or cooling rate (3°C/min) on bars obtained by unidirectional pressing and sintering in air for 2h at the required temperature. The results are summarized in Table 2.[5,14]

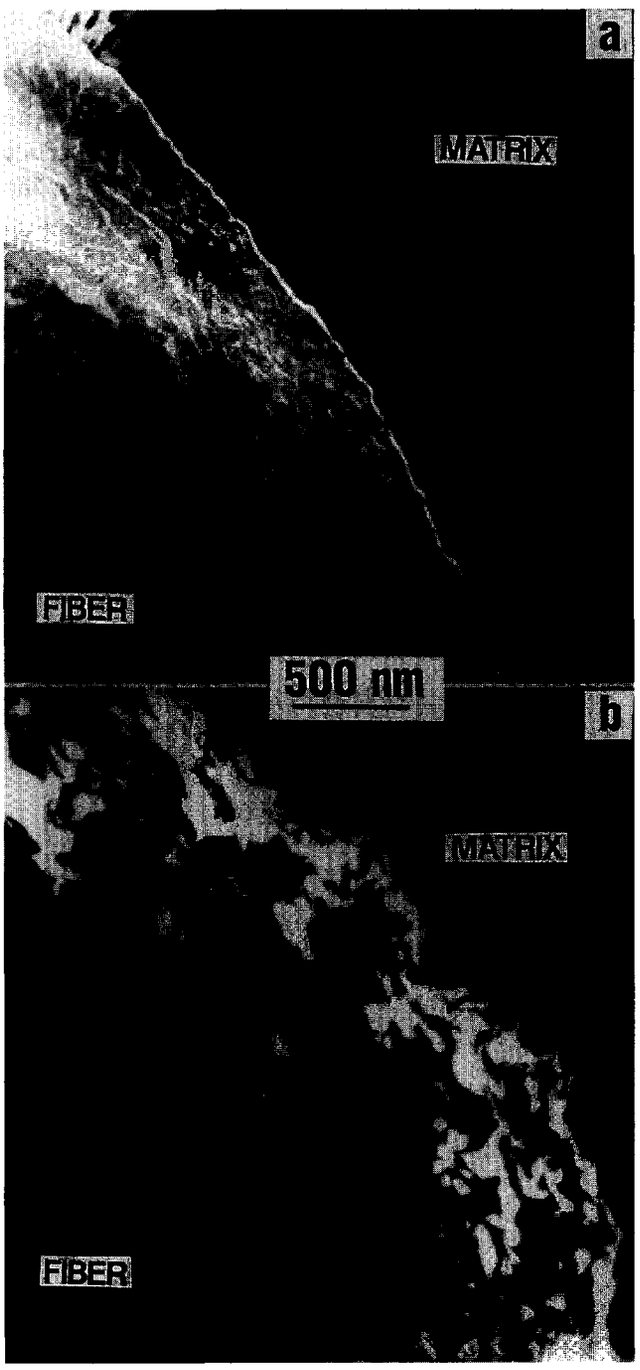

Fig. 4. P25 fibre cross-sections. Bright field TEM image, taken from fibres within the same composite (P5). The matrix appears dark. Clear areas within the fibres are isotropic parts, while dark areas are anisotropic parts; (a) and (b) are two examples of fibres with various corrugated surfaces.

It can be noted that the CTE of the glass-ceramic is lower than that of the glass, which depends on the low CTE of the cordierite. The glass transition temperature interval obtained with this technique is similar to that determined by DTA.

2.3 Composites processing

Pre-preg sheets were prepared by using a slurry infiltration process of fibre tows. The impregnated fibres are wound on a hexagonal mandrel. The volume fraction of fibres is nearly equal to 35%. After drying, the tapes were cut into 35 × 35 mm^2 pieces, stacked and debound. Then the samples were densified in argon by hot-pressing in the 950–1250°C temperature interval with a pressure of 10 MPa (LPA-DVM Goliath) followed by a linear increase or decrease in temperature (25°C/min). The unidirectional pressure was applied when the sintering temperature had been reached and was removed on cooling.

In order to optimize the density and the fracture strength of the composites, various thermal cycles have been performed. The conditions are summarized in Table 3 where, in some cases, two temperature–time combinations are given. The first corresponds to the densification step under applied pressure. The second — if any — corresponds to an additional pressureless crystallization step at a higher temperature.

3 Composites Microstructure and Properties

3.1 Density and fibre distribution

The density has been measured by the hydrostatic technique.

For the P25 fibre-reinforced composites, after hot-pressing for at least 30 min, the open porosity ranges from 1·5 to 3·7%, except for P1, which was hot-pressed at a low temperature and the open porosity of which is about 24%. Indeed, at 950°C, the viscosity of the glass is too high to allow a viscous flow in the tows. Nevertheless, some bundles of fibres were not impregnated by the glass and the distribution of the fibres in the matrix is not homogeneous (Fig. 9(a)).

The density of T400H fibre-reinforced composites increases gradually as the sintering temperature is raised up to 1150°C and the viscosity decreases. Probably due to the high number of fibres in a tow (3000), the composites always exhibit some porosity (Table 4) and non-impregnated bundles of fibres can be pulled out during polishing (Fig. 9(b)). For sintering temperatures higher than 1150°C, the porosity increases again. This latter phenomenon could be related to a release of nitro-

gen from T400H fibres. Such a release occurring when the matrix is still viscous (at 1050° for T7) is likely to prevent good adhesion between the fibres and the matrix whereas, for hot-pressing at 1150°C (T5), carbon pyrolysis is nearly achieved and the matrix can closely take the forms of the fibres. When hot-pressing occurs at 1200°C (T6), the viscosity of the matrix may become too high because of crystallization, which could prevent the impregnation of the fibres.

3.2 Matrix crystallization

X-ray diffraction equipment with a computer search/match program was used to determine the

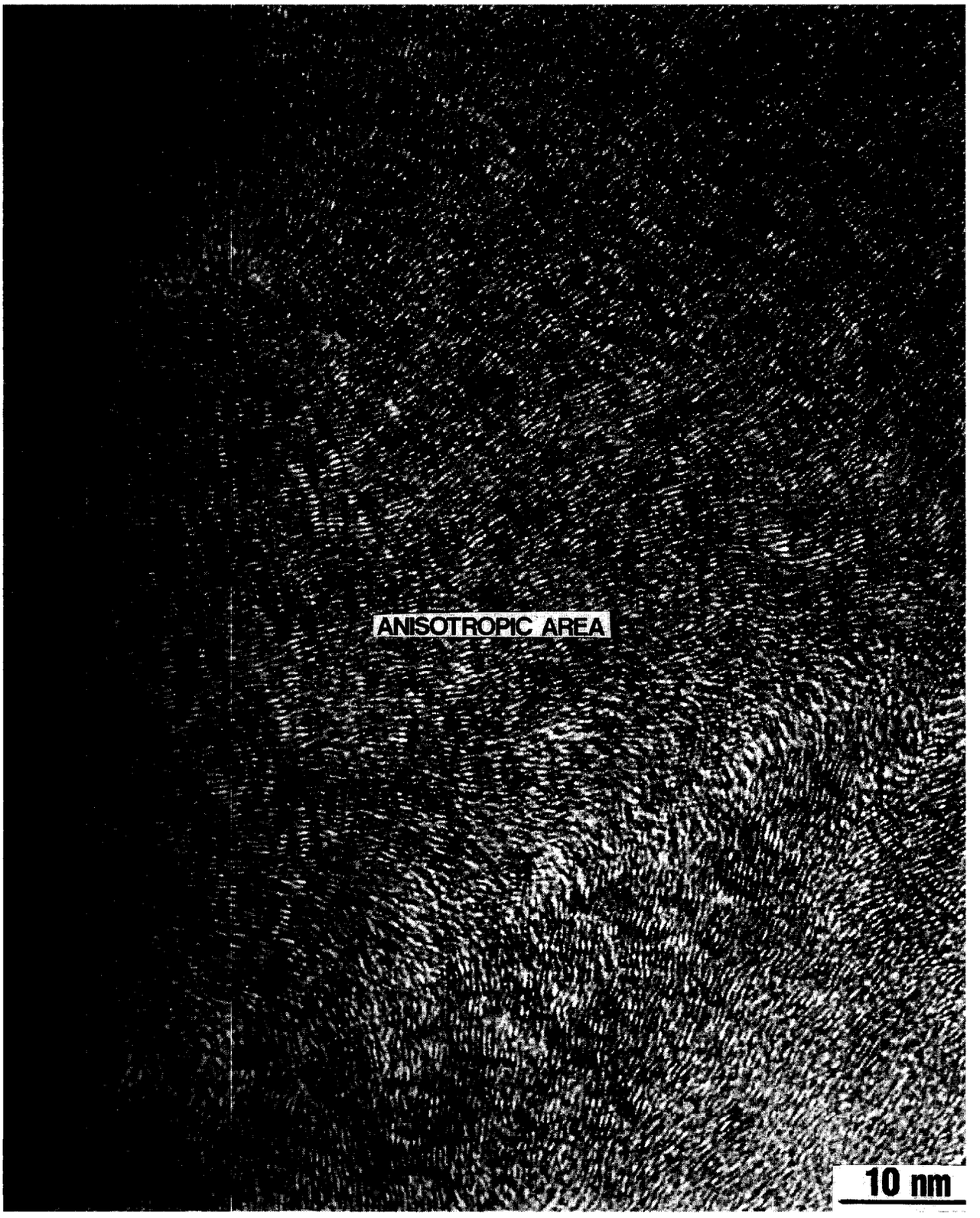

Fig. 5. P25 fibre cross-section. Lattice fringe TEM image. The comparison with Fig. 2 demonstrates the lower structural organization of P25 fibres relative to P55 fibres, while exhibiting similar textural features (anisotropic domains). Note the absence of interlayer decohesions.

nature of the phases and to follow the crystallization of the matrix versus the sintering conditions. The XRD results were obtained at room temperature from the sintered samples.

Whatever the fibres used, the microstructural changes in the matrix were similar (Fig. 10(a, b)). Up to 1000°C, X-ray diffraction patterns show that the matrix remains mainly vitreous. Only the diffraction lines of α-alumina appear, but this compound is also detected in the starting glass powder. The $MgAl_2O_4$ spinel (JCPDS 22-1152 file) precipitates above 1050°C, as well as the hexagonal high temperature cordierlite (JCPDS 13-0293 file — indialite) and the α-and β-$Y_2Si_2O_7$ yttrium silicates (JCPDS 38-0223, 38-0440 files). The SiO_2–Y_2O_3 system is very complex with many polymorphic phases in the case of $Y_2Si_2O_7$ (α, β, γ, δ). The phase transformations depend on temperature, time and impurities. The crystallization starts around 1050°C but the rate is slow and after one hour it seems to stop. At 1250°C, the α-$Y_2Si_2O_7$ turns almost completely into the β form. This result agrees with the transformation temperature indicated by Liddel and Thompson.[15] An extensive study of the structural changes occurring within the matrix with increasing temperature is being published as a companion paper.[16]

3.3 Microcracking and fracture strength of the composites

The anisotropic structure of the carbon fibre used leads to anisotropic properties. In particular this is obvious for their coefficient of thermal expansion which is close to zero along the fibre axis and about 20×10^{-6} °C^{-1} in the radial direction.[17] The thermal expansion mismatch with the matrix induces stresses on cooling. When these residual stresses are higher than the matrix strength, a network of microcracks, which are perpendicular to the fibre axis and are deflected by the fibres, can form in the matrix and are observed in the present composites. Iacocca and Duquette[18] have observed the same microcracking phenomenon in carbon-fibre-reinforced glass-matrix composites and have studied their effects on the oxidation behaviour of composites. Different models have been proposed to determine the interfacial stresses[19–25] in order to compare them with the mechanical strength of the matrix. Observation of microcracking on metallographically prepared samples showed that the cracks were regularly spaced. The average distance between neighbouring cracks changed with the hot-pressing conditions of the composites (Table 5), which means that the interfacial shear friction stress can change with the sintering temperature. The A.C.K. theory[19] allows

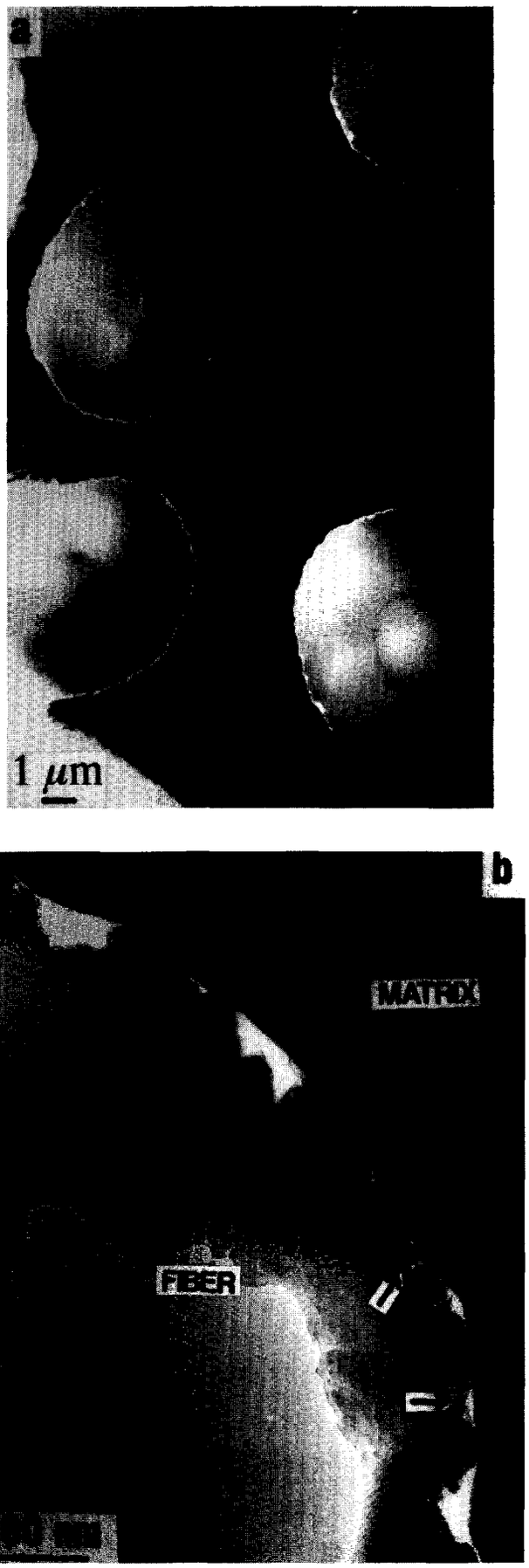

Fig. 6. T400H fibre cross-section. Bright field TEM images taken from fibres within a composite (T5).(a) Note the sizes and shapes of fibres, together with the dark ring at about one third of the fibre radius. (b) Enlargement revealing the well-corrugated fibre surface. Arrows indicate hole located close to the fibre surface.

the interfacial shear stress τ to be estimated from the distance l between microcracks :

$$l = \frac{V_m}{V_f} \cdot \frac{\sigma_{mu} \cdot r}{2 \cdot \tau} \quad (1)$$

where V_m and V_f are the matrix and fibre volume fractions, respectively, r is the radius of the fibre and σ_{mu} is the fracture strength of the matrix. It can be pointed out that the crack spacing changes less significantly for P25 fibre-reinforced composites than for T400H fibre-reinforced composites. That would indicate that, after debonding, the relative sliding movement between fibre and matrix would dissipate more or less energy. Indeed, the nature and the resistance to debonding and sliding of the fibre–matrix interface can

Fig. 7. T400H fibre cross-section. Bright field TEM image taken in the light-grey part of a fibre from Fig. 6. The presence of holes (arrow) attests that the area imaged is close to the fibre surface.

proceed from physicochemical reactions at the interface and from the thermal stresses induced by the differences between the expansion coefficients of the components. It is possible that physicochemical reactions between the P25 fibre and the matrix are different from those which occur between the T400H fibre and the matrix, since the fibres come from different precursors and have different structures.[26] Moreover, their CTE can also be different and non-linear with temperature,[14, 17] inducing different stresses in the matrix. Other parameters like the radius and the Young's modulus of the fibre influence the development of thermal stresses and matrix cracking strain. For example, with a higher fibre Young's modulus, the stress in the matrix increases. Indeed,

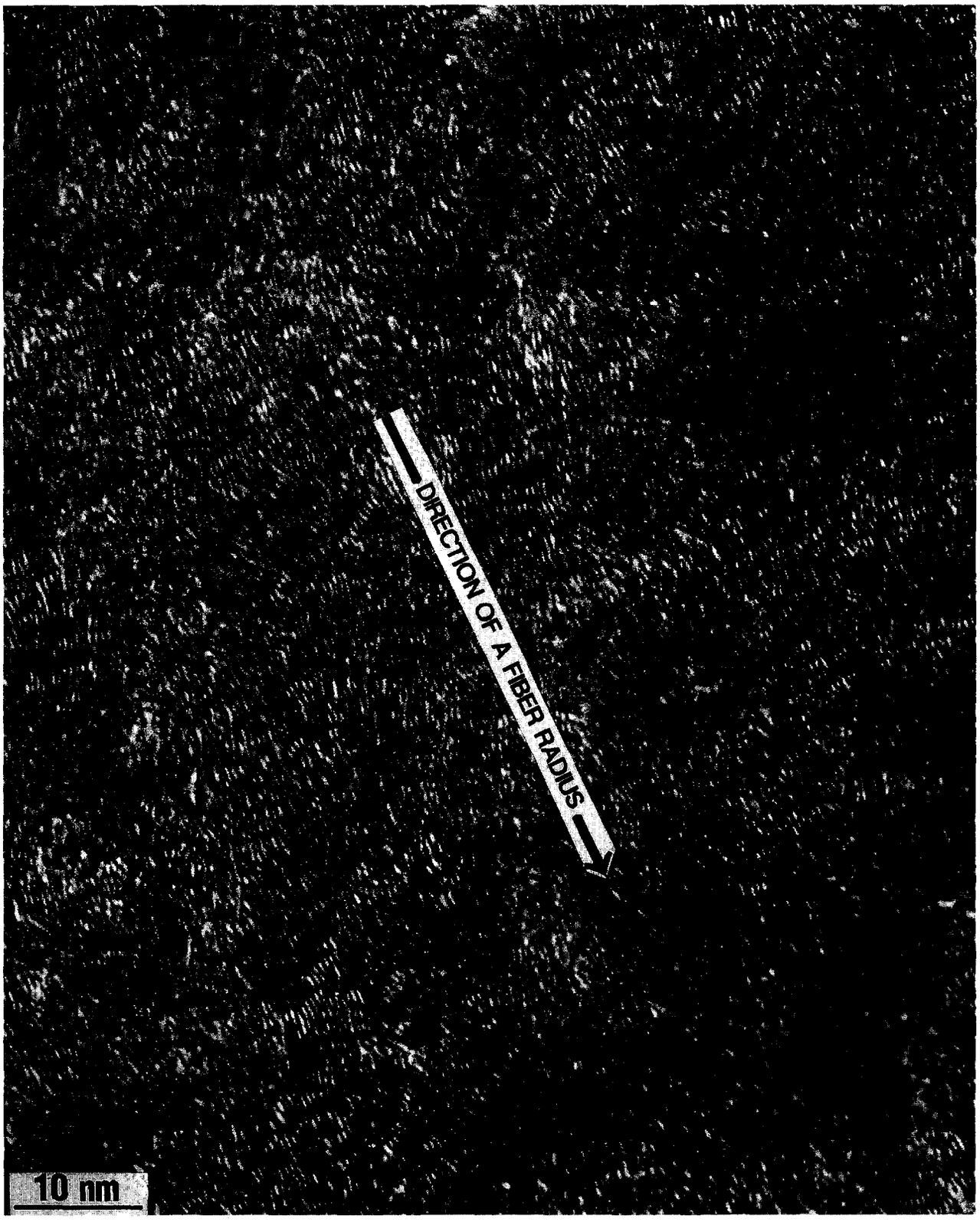

Fig. 8. T400H fibre cross-section. Bright field TEM image taken in the dark-grey ring within the fibre from Fig. 6. The distribution of the graphene stacks is highly anisotropic (they are radially oriented relative to the fibre surface).

for isotropic properties of fibres and the matrix, the thermal stress in the matrix σ_m is a function of the volume fractions (V_m and V_f), Young's moduli (E_m and E_f) and CTEs (α_m and α_f) of the matrix and the fibre and of the temperature interval:[27]

$$\sigma_m = \frac{(\alpha_f - \alpha_m) \cdot E_f \cdot V_f \cdot \Delta T}{1 + V_f \cdot (E_f/E_m - 1)} \quad (2)$$

E_f also plays a role in determining the matrix cracking stress σ_{mu}, and consequently the crack spacing, as do the radius of the fibre and the interfacial shear stress:[19]

$$\sigma_{mu} = E_c \cdot \varepsilon_{mu} = (E_m \cdot V_m + E_f \cdot V_f) \cdot \varepsilon_{mu} \quad (3)$$

$$\varepsilon_{mu} = \sqrt[3]{\frac{12 \cdot \tau \cdot \gamma_m \cdot E_f \cdot V_f^2}{E_c \cdot E_m \cdot r \cdot V_m}} \quad (4)$$

where E_c is Young's modulus of the composite and γ_m the fracture surface energy per unit volume of the matrix.

We could compare the development of the crack spacing for P25 and T400H fibre-reinforced composites as a function of parameters like the Young's modulus or the radius of the fibres, which are very different for the two grades. But these parameters cannot be considered alone, since the interfacial shear stress and the CTE also play important roles in the spacing. Moreover, eqn (2) was derived for an isotropic fibre and matrix, and is not therefore applicable to carbon

Table 2. Coefficients of thermal expansion of glass and glass–ceramic

	Sintering temperature (°C)						
	950	*1000*			*1250*		
Temperature interval (°C)	20–700	20–400	400–800	800–1000	20–400	400–800	800-1200
α (10^{-6} °C^{-1})	6.8	4.9	6.0	8.0	4.4	6.0	7.6

Table 3. P25/YMAS, P55/YMAS and T400H/YMAS processing conditions

Ref.	*Fibre*	*Sintering conditions*		*Ref.*	*Fibre*	*Sintering conditions*	
		With load	*Without load*			*With load*	*Without load*
T1	T400H	1000°C–1 h		P5	P25	1050°C–1 h	
T2	T400H	1025°C–1 h		P6	P25	1050°C–1 h	1050°C–1·5 h
T3	T400H	1050°C–1 h		P7	P25	1050°C–1 h	1050°C–6 h
T4	T400H	1100°C–1 h		P8	P25	1100°C–1 h	
T5	T400H	1150°C–1 h		P9	P25	1150°C–1 h	
T6	T400H	1200°C–1 h		P10	P25	1050°C–0·5 h	1250°C–0·5 h
T7	T400H	1050°C–1 h	1250°C–1·5 h	P11	P25	1050°C–1 h	1250°C–1·5 h
P1	P25	950°C–1 h		P12	P55	1000°C–1 h	
P2	P25	970°C–1 h		P13	P55	1050°C–1 h	
P3	P25	1000°C–1 h		P14	P55	1100°C–1 h	
P4	P25	1050°C–0·5 h		P15	P55	1150°C–1 h	

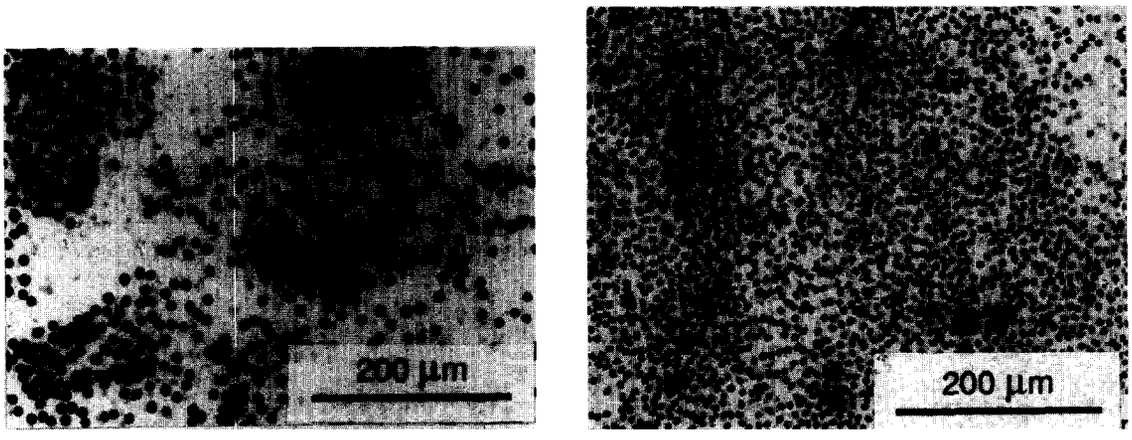

(a) (b)

Fig. 9. Distribution of fibres in matrix P5 (a) and T4 (b).

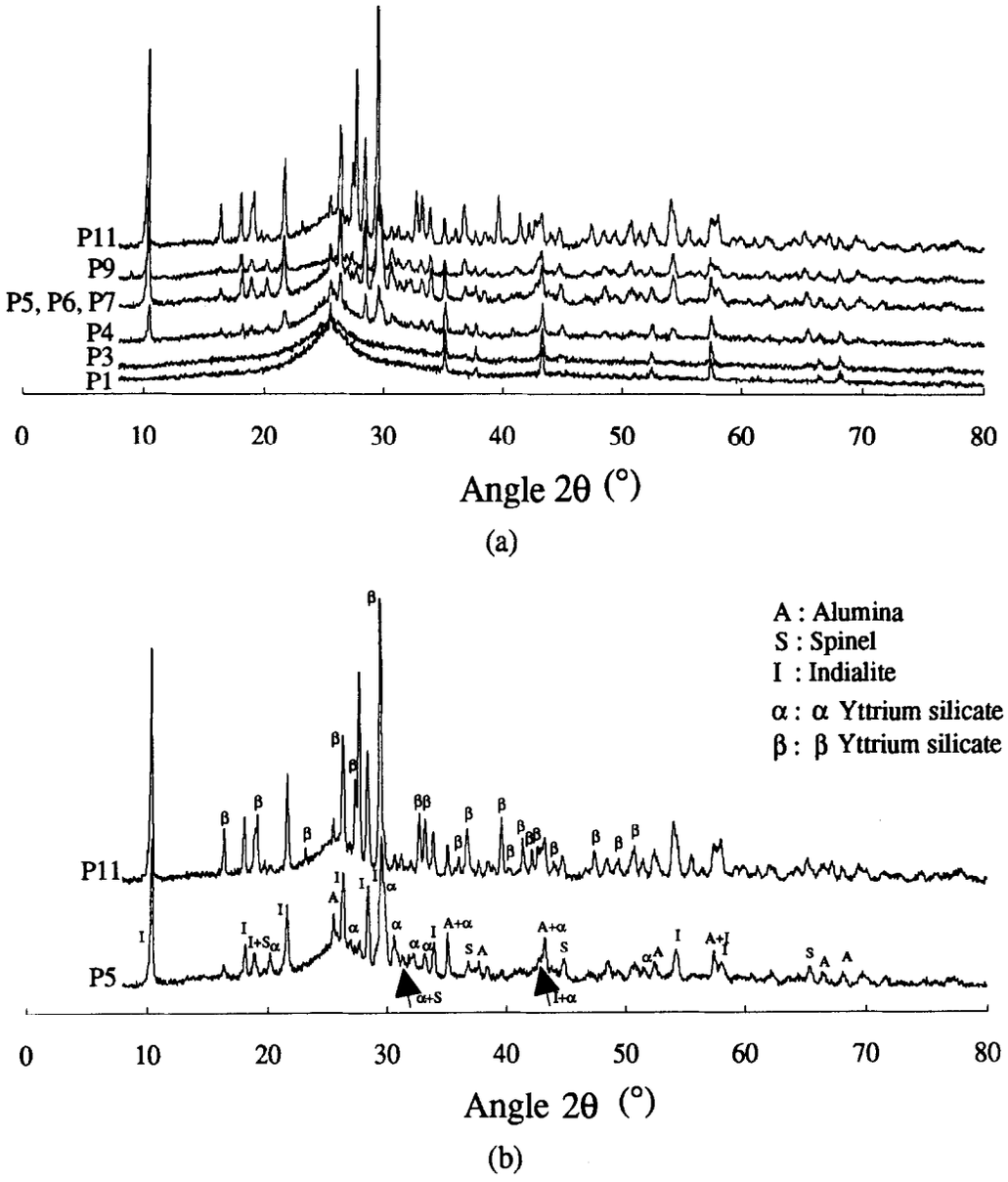

Fig. 10. (a) X-ray diffraction patterns of P25/YMAS series. (b) Identification of phases on P5 and P11 patterns.

Table 4. Open porosity (π_0) of T400H/YMAS composites (V_f is volume fraction of fibres)

	Composite						
	T1	*T2*	*T3*	*T4*	*T5*	*T6*	*T7*
V_f (%)			33·7			34·7	
π_0 (%)	15	12·4	10	7	4·5	6·7	8·3

Table 5. Microcrack spacing measured by optical microscopy in T400H and P25 fibre-reinforced composites versus their fabrication thermal cycle

Composite	*Fibre*	*Microcrack spacing (μm)*	*Composite*	*Fibre*	*Microcrack spacing (μm)*
T1	T400H	95 ± 26	P2	P25	171 ± 52
T2	T400H	104 ± 28	P3	P25	207 ± 50
T3	T400H	192 ± 34	P5	P25	279 ± 78
T4	T400H	328 ± 85	P7	P25	259 ± 83
T5	T400H	449 ± 120	P8	P25	264 ± 65
T6	T400H	397 ± 112	P9	P25	252 ± 67
T7	T400H	552 ± 148	P10	P25	603 ± 180
			P11	P25	1008 ± 270

fibres. We have already proposed a model that considers the thermo-elastic anisotropy in the calculation of thermal residual stresses.[5,14] Due to the great influence of thermal residual stresses on the mechanical behaviour of composites, we will develop this model in a subsequent paper and apply it to P25 and T400H fibre-reinforced composites.[28]

Residual thermal stresses and matrix microcracking upon cooling lead to a lower fracture strength than if microcracking occurs during the mechanical test. In the former case, the work of rupture corresponds only to elongation of the fibres, sliding inside matrix blocks and pulling-out. Then, the elastic stage and the onset of microcracking in the matrix cannot be observed on load–deflection curves. If a change in the slope occurs for low loads, it is a priori only due to widening of the cracks before the beginning of fibre sliding.

Three-point bend tests were performed on bars ($34 \times 6 \times 1{\cdot}5$ mm^3) at room temperature, with a span of 30 mm and a loading rate of 0.2 mm/min. Typical load–deflection curves of P25 and P55 fibre-reinforced composites are reported in Fig. 11(a) and (b). For both grades of fibre, all the composites exhibit the same non-brittle behaviour and the same fracture strength, which is about 440 ± 60 MPa with P25 fibres (volume fraction 35%), and 390 ± 50 MPa with P55 fibres (volume fraction 35%). Observation of fracture surfaces shows fibre extractions about 100 μm long for P25/YMAS composites hot-pressed at a temperature lower than 1150°C (Fig. 12(a)). For samples crystallized at 1250°C (Fig. 12(b)), fibre extraction lengths are about 1 mm long, which is consistent with the significant increase in the distance between microcracks and in agreement with TEM observations of the fibre–matrix interface and fibre micro-indentation tests.[5,14,26] Indeed, a wider interfacial separation has been shown for samples crystallized at 1250°C and both the interfacial debonding and shear stresses have been proved lower in this case.

In contrast, the fracture behaviour of T400H/YMAS composites varies with the sintering conditions (Fig. 13), which means that some changes occur in residual thermal stresses and interactions between the fibres and the matrix. We have already demonstrated[5,14] that both effects lead to these different fracture behaviours. Radial and axial thermal stresses have been calculated for T400H fibre-reinforced composites and have allowed, with some assumptions, the beginning of matrix microcracking and fibre debonding to be explained for some sintering temperatures.

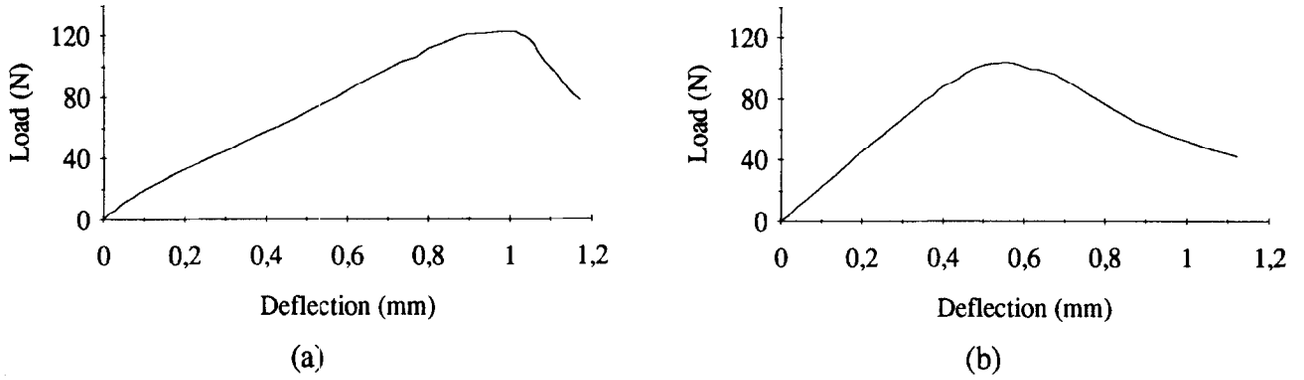

Fig. 11. Load–deflection curves (three-point bend test) (a) of a P25/YMAS composite (P5) and (b) of a P55/YMAS composite (P14).

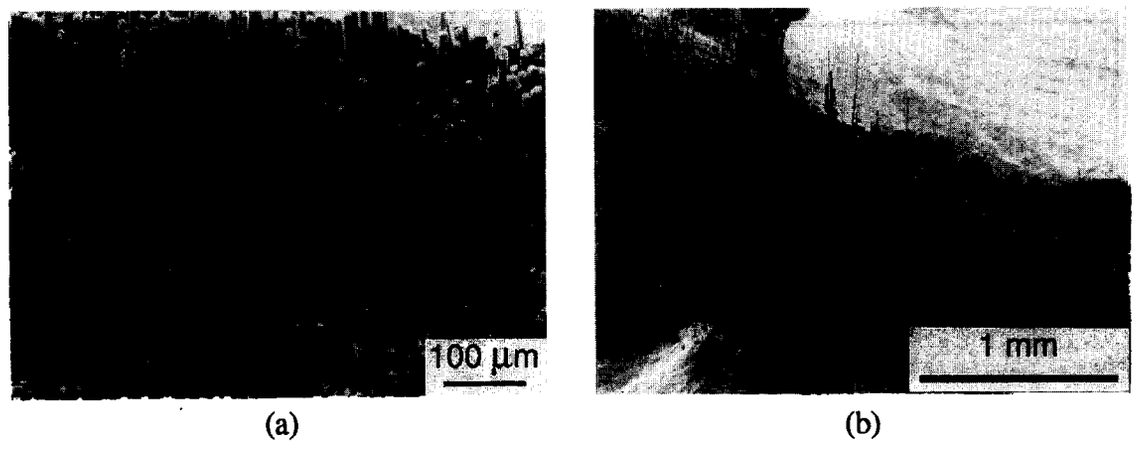

Fig. 12. Surface fractures of some P25/YMAS composites: composite P5 (a) and composite P11 (b).

As the hot-pressing temperature is raised to 1150°C, the ultimate strength increases with a maximum value at 1150°C ($\sigma_r \approx$ 1100 MPa). The fibre–matrix friction stress is weaker, some decohesions at the interface are observed by TEM,[5,14,26] which explains the higher average distance between cracks. Except for the samples T1 and T7, the brittle rupture seems inconsistent with the appearance of the fracture surfaces (Fig. 14(c)) where debonded fibres are seen. The brittle behaviour might be related to Weibull's modulus of the T400H fibres, but also to the grooved surface texture which can inhibit the debonding. The low fracture strength of the T1 composite seems to be due to the strong cohesion between the fibre and the matrix, except in some bundles of non-impregnated fibres which can be extracted easily and can explain the non-catastrophic rupture of this composite (Fig. 14(a) and (b)). The strong cohesion has also been proved by TEM observations[5, 14, 26] which permitted a determination of the nature and structure of the interface. For hot-pressing temperatures higher than 1150°C, the fracture strength decreases, suggesting changes in the fibre–matrix bond. The length of the debonded fibres is similar but the average distance between microcracks indicates that the interfacial shear stress is lower. These observations suggest that the decrease in the fracture strength is due to a delamination process. The long distance between microcracks gives rise to wide microcracks. When the load is applied during the flexural test, the width of the cracks leads to delamination and some bundles of fibres are easily extracted (Fig 14(d)).

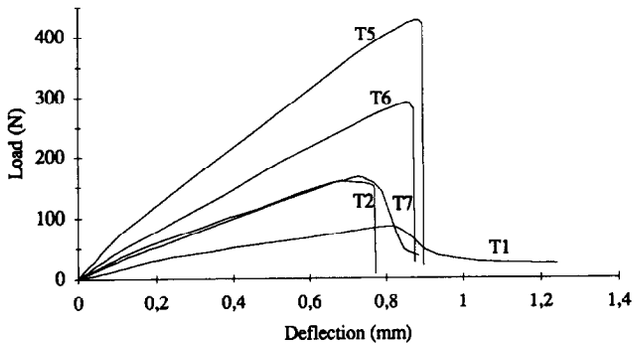

Fig. 13. Load–deflection curves (three-point bend test) of T400H/YMAS composites.

4 Conclusion

The mechanical behaviour of carbon-fibre-reinforced YMAS composites depends strongly on the carbon fibres used and the hot-pressing conditions of the

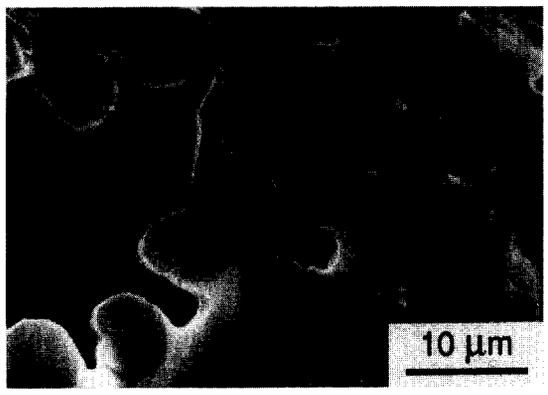

(a)

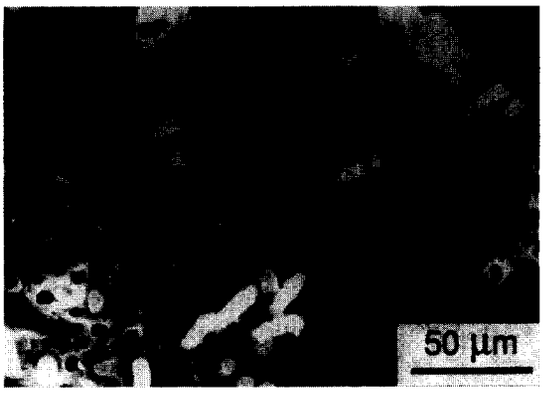

(b)

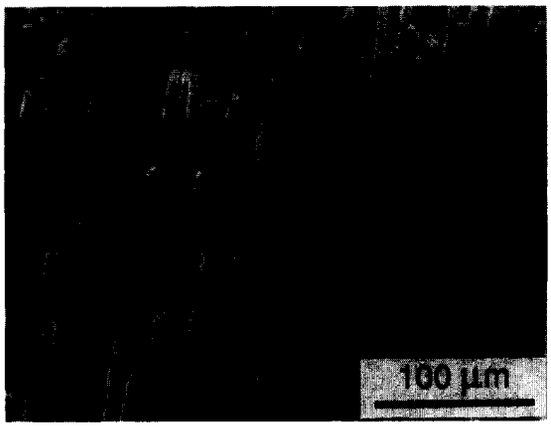

(c)

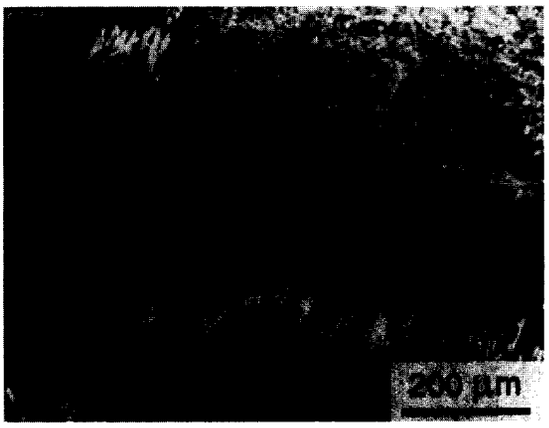

(d)

Fig. 14. Surface fractures of some T400H/YMAS composites: composite T1 (a and b), composite T5 (c) and composite T7 (d).

matrix. The micro-texture and structure of carbon fibres and their thermomechanical properties differ depending on the precursor, the preparation and the sintering conditions. In the same way, both microstructure and final properties of the matrix change with temperature. Therefore, the fibre–matrix bond, which is well-known to govern to a large extent the fracture strength of composites, is influenced by all these changes.

For pitch-based carbon-fibre-reinforced composites, the fracture is always controlled, suggesting that the interfacial bond is relatively weak, and there is no noticeable evolution in the ultimate fracture strength. Nevertheless, when the hot-pressing temperature is increased from 950°C to 1250°C and the glass matrix becomes crystallized, fibre extractions and the interval between microcracks increase. Both observations suggest changes in the interfacial shear stress with the sintering conditions. The highly anisotropic but incomplete polyaromatic carbon skin of the fibres may play a role in the nature and strength of the fibre–matrix bond. Indeed, the stiff layers at the surface of the fibre have a low reactivity[29] and could lead to a weak chemical bond between the fibres and the matrix.

In the case of T400H fibre-reinforced composites, the fracture strength varies markedly with the sintering conditions which indicates changes in thermal residual stresses and/or physicochemical reactions between the fibre and the matrix. Up to the 1150°C hot-pressing temperature, the ultimate strength increases and the rupture remains brittle, except if the temperature is too low and prevents some bundles of fibres being adequately impregnated. For temperatures higher than 1150°C, the fracture strength of the composites decreases, the rupture is less brittle due to both the effects of a weaker interfacial shear strength and delamination.

For all the composites, at high process temperatures, the oxidation of the fibres by the matrix plays a non-negligible role on the fibre–matrix interface. Due to the importance of the fibre–matrix interface characteristics, a subsequent paper will be devoted to these particular aspects.[26]

References

1. Nardone, V. C. and Prewo, M., Tensile performance of carbon-fibre-reinforced glass. *J. Mater. Sci.*, 1988, **23**, 168–180.
2. Prewo, K. M., Carbon fibre reinforced glass matrix composite tension and flexure properties. *J. Mater. Sci.*, 1988, **23**, 2745-2752.
3. Hegeler, H. and Brückner, R., Mechanical properties of carbon fibre-reinforced glasses. *J. Mater. Sci.*, 1992, **27**, 1901–1907.
4. Seraudie, C., Elaboration et propriétés thermomécaniques de composites à fibres de carbure de silicium et matrices vitrocéramiques. PhD thesis, Limoges University, France, 1990.
5. Bianchi, V., Composites à fibres de carbone et matrice YMAS: elaboration, microstructure, comportements mécanique et tribologique. PhD thesis, Limoges University, France, 1995.
6. Després, J. F. and Monthioux, M., Etude des interfaces des composites C/C/SiC, relation avec les propriétés mécaniques. Internal Report to Société Européenne de Propulsion, Bordeaux, 1992.
7. Després, J. F., Les interphases de carbone pyrolytique dans les composites carbone/carbure de silicium. PhD thesis, Pau and Pays de l'Adour University, France, 1993.
8. Guigon, M., Oberlin, A. and Désarmot, G., Microtexture and structure of some high tensile strength, PAN-based carbon fibres. *Fibre Sci. Technol.*, 1984, **20**, 55–72.
9. Sinkler, W. and Monthioux, M., Etude de composites à renfort carbone et matrice verre de type B. Internal Report to Céramiques et Composites, Tarbes, 1994.
10. Guigon, M. and Oberlin, A., Preliminary studies of mesophase-pitch based carbon fibres: structure and microtexture. *Compos. Sci. Technol.*, 1986, **25**, 231–241.
11. Oberlin, A., High resolution TEM studies of carbonization and graphitization. In *Chemistry and Physics of Carbon*, vol 22, ed. P. A. Thrower. Marcel Dekker, New York, 1989, pp. 1–142.
12. Lafdi, K., Bonnamy, S. and Oberlin, A., Anisotropic pitch-based carbon fibers. Carbonization and graphitization (radial-with-edge I1 and radial I2 types). *Carbon*, 1992, **30**, 533–549.
13. Lamouroux, F., Bourrat, X., Naslain, R. and Sévely, J., Structure oxidation behavior relationship in the carbonaceous constituents of 2D-C/PyC/SiC composites. *Carbon*, 1993, **31**, 1273–1288.
14. Bianchi, V., Goursat, P., Ménessier, E., Sinkler, W. and Monthioux, M., C/YMAS composites — Effects of the interface and the residual stresses on the rupture behaviour. In *Advanced Structural Fiber Composites, Advances in Science and Technology*, ed. P. Vincenzini, vol.7, 1994, pp, 695–702.
15. Liddel, K. and Thompson, D. P., X-Ray diffraction data for yttrium silicates. *Br. Ceram. Trans. J.*, 1986, **85**, 17–22.
16. Sinkler, W., Monthioux, M., Bianchi, V., Goursat, P. and Ménessier, E., Carbon fiber-reinforced (YMAS) glass–ceramic matrix composites. II. Structural changes in the matrix with temperature. *J. Eur. Ceram. Soc.*, to be submitted.
17. Menessier, E., Dumont, J. P., Guette, A., Pailler, R., Rabardel, L. and Naslain, R., Axial and radial coefficients of thermal expansion of carbon fibers in the 20–430°C temperature range as derived from the thermal expansion of I-D-C-SiO_2 (B_2O_3) composites. *Ceram. Eng. Sci. Proc.*, 1989, **10**, 1426–1439.
18. Iacocca R. G. and Duquette, D. J., The effects of matrix microcracking on the oxidation behaviour of carbon-fibre/glass-matrix composites. *J. Mater. Sci.*, 1993, **28**, 4749–4761.
19. Aveston, J., Cooper, G. A. and Kelly, A., The properties of fibre composites: single and multiple fracture. In *Conference Proceedings*, Natl Phys. Lab., Teddington, UK, 1971, pp. 15–26.
20. Budianski, B., Hutchinson, J. W. and Evans, A. G., Matrix fracture in fiber-reinforced ceramics. *J. Mech. Phys. Solids*, 1986, **34**, 167–189.
21. Sutcu, M. and Hillig, W. B., The effects of fiber–matrix debond energy on the matrix cracking strength and the debond shear strength. *Aca Metall. Mater.*, 1990, **38**, 2653–2662.
22. Pérès, P., Analyse théorique et expérimentale du rôle des paramètres de microstructure sur le comportement des

composites à matrice fragile. PhD. thesis, INSA, Université de Lyon, France, 1988.
23. Lamon, J., Lissart, N. and Rechiniac C., Micromechanical and statistical approach to the behaviour of CMCs. *Ceram. Eng. Sci. Proc.*, 1993, **14**, 1115–1124.
24. Marshall, D. B., Cox, B. N. and Evans, A. G., The mechanics of matrix cracking in brittle matrix fiber composites. *Acta Metall. Mater.*, 1985, **33**, 2013–2021.
25. McCartney, L. N., Mechanics of matrix cracking in brittle matrix fibre reinforced composites. In *Proc. R. Soc. Lond.* 1987, **A409**, 329–350.
26. Bianchi, V., Goursat P., Sinkler, W., Monthioux, M. and Ménessier, E., Carbon fiber-reinforced (YMAS) glass-ceramic matrix composites. III. Interfacial aspects. *J. Eur. Ceram. Soc.*, to be submitted.
27. Aveston, J., The properties of fibre composites: strength and toughness in fibre-reinforced ceramics. In *Conference Proceedings,* Natl Phys. Lab., Teddington, UK, 1971, pp. 63–73.
28. Bianchi, V., Goursat P. and Ménessier, E., Carbon fiber-reinforced (YMAS) glass–ceramic matrix composites. IV. Thermal residual stresses and fiber/matrix interfaces. *J. Eur. Ceram. Soc.*, to be submitted.
29. Donnet, J. B., Structure and reactivity of carbons: from carbon blacks to carbon composites. *Carbon*, 1982, **20**, 267–282.